Specular X-ray Reflectivity and Small Angle Neutron Scattering for Structure Determination of Ordered Mesoporous Dielectric Films

Bryan D. Vogt,* Hae-Jeong Lee, and Wen-li Wu

Polymer Division, National Institute of Standards and Technology, Gaithersburg, Maryland 20899

Youfan Liu†

Intel Assignee at SEMATECH, Austin, Texas 78741

Received: May 16, 2005; In Final Form: July 12, 2005

Specular X-ray reflectivity (SXR) and small-angle neutron scattering (SANS) are used to characterize the structure of a thin film containing cylindrical mesopores. The 3-D structure of the mesoporous film was determined from SANS measurements taken at multiple rotation angles between the incident beam and the film. The film was found to be composed of a randomly packed core and surface layers within which the hollow cylinders were regularly packed and oriented along the surface. The packing of the cylindrical mesopores was not hexagonal but rather rectangular with a conical angle of 55.7° instead of 60° expected for hexagonal packing. The extent of the planar orientation of the cylindrical mesopores within the surface layers was estimated from the width of the Bragg reflection in the SXR result to be about 25 repeating layers at both interfaces. This was further confirmed from cross-section transmission electron microscopy (TEM) results. The SXR results of this film exhibit an anomalous decrease in reflected intensity after each Bragg reflection. This anomaly in SXR can be modeled in a Parratt formulism using a depth profile composed of two characteristic lengths, the repeating distance among layers and the curvature of the density profile of each layer.

Introduction

Porous materials have garnered significant attention for a range of applications including catalytic, ion exchange, separation, and low dielectric constant (k) materials. For many of these applications, well-defined and ordered pores are advantageous.[1] Of particular interest has been the evolution of new mesoporous materials created using sacrificial templates since the discovery of MCM-41.[2] The pore size and space group of these materials can be controlled through the choice of self-assembling template materials[3] for a variety of metal oxide frameworks.[4] Variations based on this versatile approach have been used successfully to create mesoporous films with regularly packed pores.[5]

To control pore orientation, methods have been developed for directed growth of oriented mesoporous films from solution.[6] The orientation of these self-assembled nanostructured materials is similar to those observed in block copolymer films.[7] Because of preferential wetting of a component of the templating agent,[8] the film interfaces provide local orientation sites.[5] The depth of the orientation is typically determined from cross-sectional scanning electron microscopy (SEM) or transmission electron microscopy (TEM) images.[9] There are also numerous methods by which mesoporous materials are characterized including classic N_2 adsorption,[3,4,10] powder X-ray diffraction (XRD),[3,4,9] TEM,[3,4,9] SEM,[3,9] nuclear magnetic resonance (NMR) spectroscopy,[10] small-angle neutron scattering (SANS),[11] and grazing incidence small-angle X-ray scattering (GISAXS).[12] Primary results from these measurements have been the porosity, pore dimensions and shape, and space group for the ordered pores. One problem has been that unambiguous pore sizes cannot be obtained from the NMR or N_2 adsorption experiments—assumptions regarding the freezing of water within the pores or capillary condensation models must be made.[13] TEM allows for direct imaging of the pores, but the technique is destructive. Small-angle scattering (SANS and GISAXS) is an attractive alternative as a nondestructive characterization tool for mesoporous materials. These techniques have been successfully applied in several situations such as in situ monitoring formation of mesoporous materials with GISAXS[12] and direct observation of N_2 pore filling using SANS,[11] but these did not fully exploit the wealth of information that can be obtained from small-angle scattering.

In this paper, we describe the characterization of an ordered mesoporous film using a combination of SANS and specular X-ray reflectivity (SXR). These techniques are generally considered complementary with different spatial directions being probed; typically, SANS probes in the $x-y$ plane, while SXR examines the z-direction, where z is normal to the film and the $x-y$ plane is parallel to the film surface. SANS can be used to elucidate information along the z-direction as well as when measurements are performed at different incident angles in reference to the film surface.

Experimental Procedures

The mesoporous film was prepared by spin-coating on a silicon wafer. The films were baked on a hot plate for 1 min at 120 °C and cured in a furnace for 60 min at 400 °C under N_2 at ambient pressure. Transmission electron microscopy (TEM) was used for direct imaging of the mesoporous film using an FEI Co. TECNAITM F30 ST, 300 kV instrument. Cross-sectional samples were prepared for TEM by an epoxy-sandwich method common in the semiconductor industry, but with a 3

* Corresponding author. E-mail: bryan.vogt@nist.gov.
† Present address: Intel Corporation, Chandler, AZ.

10.1021/jp0525641 CCC: $30.25
Published on Web 09/13/2005

nm platinum layer cold-sputtered to delineate the low-k film surface followed by a 100 nm thick chemical-vapor deposited (CVD) SiO_2 layer added for strength. Final thinning of the cross-sectional sample was conducted in a Gatan Inc. PIPSTM ion-mill with 3 kV Ar^+ ions and a low-milling angle of 3.5°. A plan-view TEM sample was prepared similarly but with only a thin 5 nm TEOS cap (for strength, and no platinum), with all polishing and ion milling from the wafer side. TEM imaging for the cross-sectional sample was done with the electron beam aligned parallel to the substrate Si ⟨110⟩.

Specular X-ray Reflectivity (SXR). At X-ray wavelengths of a few tenths of a nanometer, the refractive index of materials is less than one, resulting in a critical angle below which the total internal reflection of the radiation takes place.[14] This critical angle, θ_c, can be approximated by $(\rho r_e \lambda^2/\pi)^{0.5}$, where ρ is the electron density of the material, λ is the X-ray wavelength, and ρ_e is the classical electron radius (2.818 fm). The angle is defined as the grazing angle measured from the surface parallel. Specular data are collected with the grazing incident angle equal to the detector angle. By modeling the SXR result with a 1-D Schrödinger equation in a Parratt formulism,[15] the details of the electron density depth profile can be deduced. Free-surface roughness, interfacial roughness, and density variations normal to the film surface are determined using electron-density depth profiles that best fit the experimental data.[15] The information from SXR is a lateral average over several micrometers as dictated by the coherence length of the X-ray beam.[16]

Two different instruments were used to obtain SXR data. High-resolution measurements were conducted in a $\theta-2\theta$ configuration with a fine focus copper X-ray tube. The incident beam was conditioned with a four-bounce germanium [220] monochromator. Before the detector, the beam was further conditioned with a three-bounce germanium [220] channel cut crystal. This configuration results in a copper $K_{\alpha 1}$ beam with a fractional wavelength spread of 1.3×10^{-4} and an angular divergence of 12 arc s. The motion of the goniometer is controlled by a closed-loop active servo system with an angular reproducibility of 0.0001°. These high precision settings in both the X-ray optics and the goniometer control are necessary to detect the very narrowly spaced interference fringes from films on the order of one μm thick. Lower resolution measurements were conducted in a $\theta-\theta$ configuration using Ni filtered Cu K_α radiation ($\lambda = 1.54$ Å) and a detector with a 20 eV energy window. Interference fringes from films greater than 150 nm thickness cannot be resolved with this instrument. In both instruments, a slit collimation was used, and the beam divergence referred to previously is not valid along the slit axis, defined as the *y*-axis.

Small-Angle Neutron Scattering (SANS). The small-angle neutron scattering measurements were conducted on the NG1 instrument at the Center for Neutron Research at the National Institute of Standards and Technology. Small angle neutron scattering was initially performed on thin film samples in a typical configuration with the beam incident along the surface normal. The wavelength, λ, was 6 Å with a wavelength spread, $\Delta\lambda/\lambda$, of 0.12. The sample to detector distance was 3.84 m. The resultant scattering vector, q, ranged from 0.01 to 0.18 $Å^{-1}$.

To obtain 3-D structural information, SANS data were collected with the sample surface rotated with respect to the incident beam as well as at the normal incident angle. The maximum tilt in this paper is 75°. Since the silicon wafer substrate supporting the porous film is transparent to neutrons even at a high tilt angle and the wafer does not cause any scattering in the angular range of interest, the scattered intensities in the small-angle region (less than 5°) are exclusively from the porous film. 2-D scattering intensity data were collected from each incident angle.

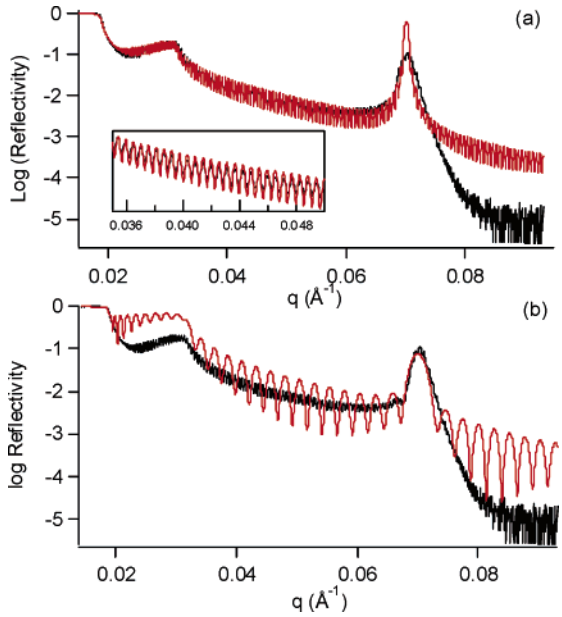

Figure 1. High-resolution specular X-ray reflectivity of mesoporous film (black lines). The reflectivity is fit to a series of repeating layers (red lines). (a) The number of repeat layers in the fit is 107. The fit faithfully captures all the low q data as shown in the inset, but the width and height of the Bragg peak is not well-represented. (b) The number of repeat layers is reduced to 25. The low q region is not well-represented by this fit, but the Bragg peak width and height corresponds to the fit. However, in both cases, the precipitous drop in reflected intensity after the Bragg reflection cannot be fit with this model.

Results

Specular X-ray reflectivity of the ordered mesoporous film is shown in Figure 1. The reflectivity profile exhibits two critical edges: the first, at $q \approx 0.02$ $Å^{-1}$, corresponds to the average density of the mesoporous film, and the second corresponds to the substrate density, silicon, at $q \approx 0.03$ $Å^{-1}$. Because of the high resolution of the reflectometer, small oscillatory Kiessig fringes are observed resultant from the total film thickness of (1004 ± 3) nm. (The data throughout the paper and in the figures are presented along with the standard uncertainty ($\pm$) involved in the measurement based on one standard deviation. The error in the thickness determined from reflectivity is from the goodness of the fit.) One additional feature is present in the reflectivity result, a Bragg reflection near 0.0676 $Å^{-1}$ resulting from the periodic density fluctuations in the film from the ordered mesopore layers with a period of approximately 93 Å. Up to the Bragg reflection, the reflectivity can be well-represented in the low q region by a film consisting of 107 repeating layers with a repeat distance of 93 Å as shown in Figure 1a. The Bragg peak location is well-represented, but the height and width of the Bragg peak do not agree with the model. Additionally, there is a dramatic decrease in the reflected intensity following the Bragg peak, and this is not captured by the previously mentioned simple model fit. The width of the Bragg peak can be modeled using the Scherrer equation commonly used in X-ray diffraction for determining crystal size. As the size of the crystal decreases, the width of the Bragg reflections increases. The same was applied to determine the total thickness of the ordered layers in the mesoporous sample. SXR is only sensitive to density fluctuations along the film

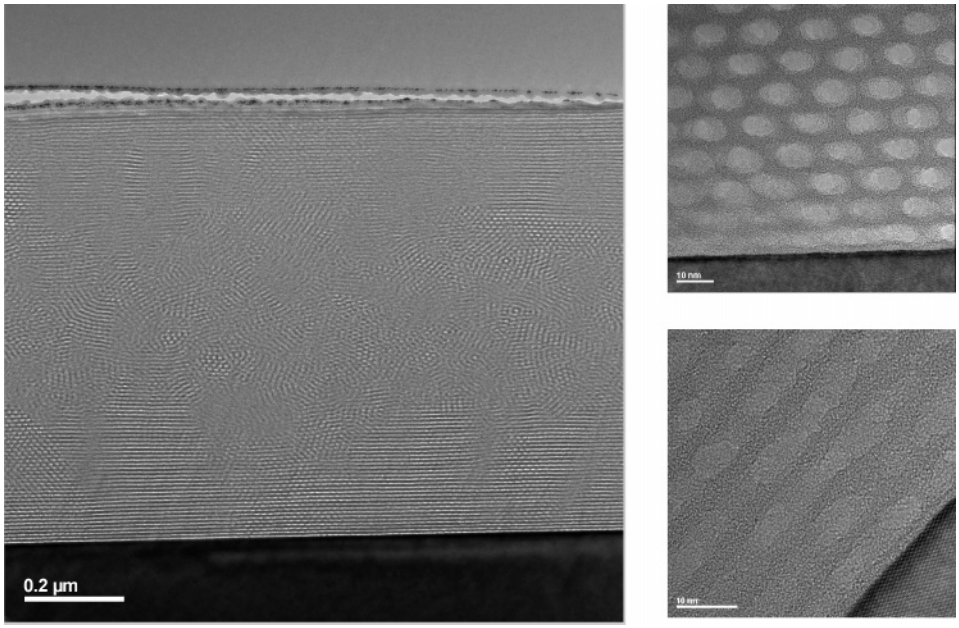

Figure 2. Cross-sectional TEM micrograph of the mesoporous film. The micrograph corroborates the interpretation of the SXR data where cylindrical pores are aligned parallel to the substrate near both interfaces. The high-resolution TEM micographs confirm the cylindrical porous nature of the film.

thickness direction, so the thickness of the ordered layers actually corresponds to the number of layers that are oriented in-plane. The width of the Bragg reflection can be fitted by decreasing the number of repeating layers to 25 with a thickness of 93 Å each. This is the crystal grain size oriented along the film surface normal analogous to the information on crystal size from X-ray diffraction using the Scherrer equation. However, both interfaces should induce orientation in the film. Thus, the average crystal size from both interfaces should be approximately 25 layers. This leaves 504 nm of an interior region where orderly packing is absent. This is confirmed with cross-sectional TEM (Figure 2), which shows preferential pore orientation near both interfaces, with the orientation extending approximately 20 layers from the free interface and approximately 30 layers from the substrate, consistent with the SXR results.

There is another discrepancy between the data and the fit of the SXR data that cannot be as easily explained: the precipitous drop in reflected intensity following the Bragg peak. Figure 3 shows the reflectivity for the film out to q of 0.35 $Å^{-1}$ using a lower resolution instrument. Two Bragg reflections are visible in the reflectivity. The ratio between the Bragg peaks is closely consistent with a hexagonal packing order. After each peak, there is a conspicuous drop in reflected intensity. In modeling the SXR data in Figure 1b, a layered structure with an error function to describe the electron density profile between the solid layer and the porous layer is assumed. To improve the fit, details of the layered structure within the film were considered and modeled as follows.

Recently, Ruland and Smarsly modeled the X-ray scattering of a similar type of film with hexagonally packed cylinders aligned parallel to the surface with the framework of Raleigh scattering. They illustrated that scattered intensity along the surface normal could be adequately fitted with a model given in the following equation:[17]

$$R(q) \propto \Phi_R{}^2(q)\frac{|Z|^2(q)}{\langle N\rangle} \qquad (1)$$

where $\Phi_R{}^2(q) = (R/q)J_1(2\pi Rq)$ is the shape factor for a cylinder

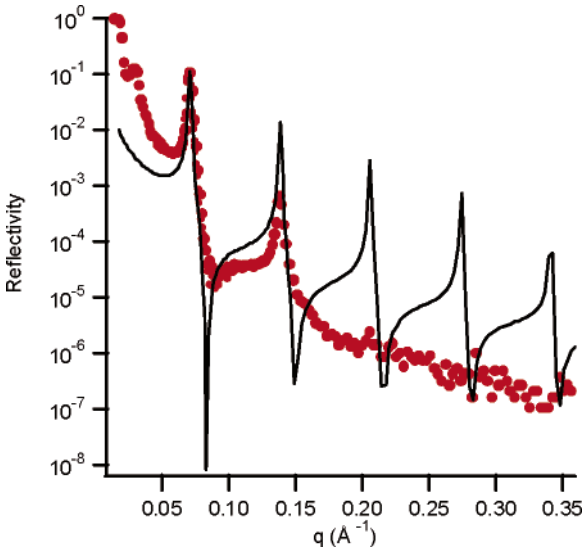

Figure 3. Red dots: low-resolution specular X-ray reflectivity of mesoporous film shows two Bragg reflections. The drop in intensity following the first Bragg peak can be qualitatively fit by considering the radius of the cylinder along with the d spacing of the unit cell (solid line).

of radius R, J_1 is the Bessel function of the first kind of order one, Z is the lattice structure factor, and $\langle N\rangle$ is the average number of unit cells. Here, we neglect details such as the variations in cylinder radius, the lattice constant, and the instrumental resolution. The previous equation can qualitatively describe the decrease in intensity immediately after each Bragg reflection as shown in Figure 3. This is due to the interference between $\Phi(q)$ and $Z(q)$. $\Phi(q)$ is a function of the cylinder radius, and $Z(q)$ is a function of the lattice parameters. The difference in the length scales invoked in these two functions results in the interference observed. Since Raleigh scattering was used in their calculation, it is not a surprise that the fit works well only in the high q regime after the silicon critical angle. In this paper, we demonstrate that two length scales can be included in the model for SXR data as well. This is in contrast to the approach resulting in Figure 1a where a simple multilayer model is used.

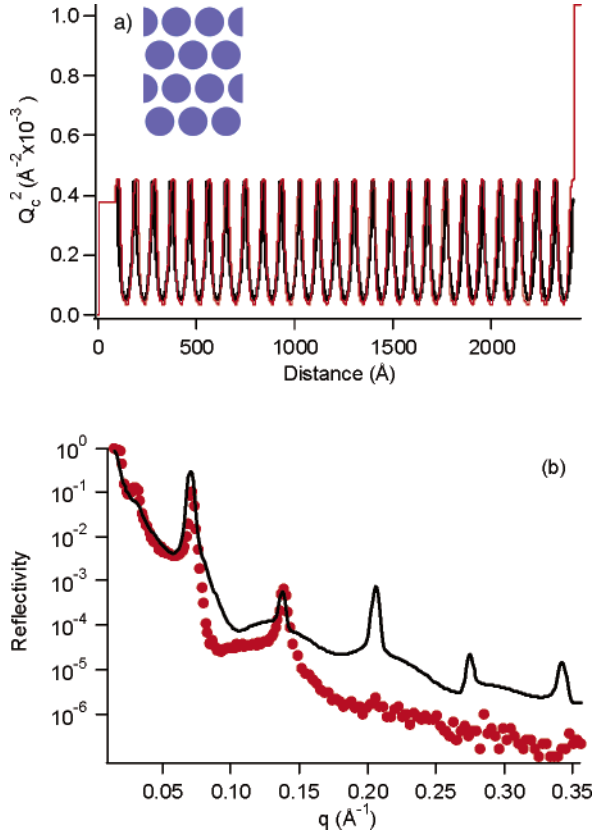

Figure 4. Pore structure of idealized film (inset in panel a) used to create the scattering length density profile (a) that can be used in the Parratt formulism[15] to fit the reflectivity data (b). The black line in panel a corresponds to the 1-D density profile of the inset idealized film. The red line is the density profile created from 25 repeats of a 10 layered structure that replicates the calculated profile used in panel b. The cylinder length scale manifests itself as the curvature between the high and the low scattering length density regions.

The repeat used for the lattice factor $Z(q)$ is 93 Å, corresponding to the position of the Bragg peak in Figure 1. $\langle N \rangle = 25 \pm 10$ is used in eq 1, based on the SXR result and the TEM micrograph. The other length scale is the cylinder radius, and a value of 41 Å was assigned. We will return to the origin of this value for a cylinder radius later. In the following, we will demonstrate that by introducing these two length scales in the traditional Parratt formalism, one can improve the fit to include the regime before the first Bragg peak. In the traditional Parratt fit of reflectivity data,[15] the film is modeled with a 1-D profile that describes the in-plane averaged depth profile of the film in terms of its electron density. To begin, we used an idealized structure consisting of infinite cylinders all aligned parallel to one another with $R = 41$ Å, and d spacing $= 93$ Å on a hexagonally packed lattice is used to construct the electron density profile as illustrated in Figure 4a. The cylinder does not introduce a discrete layer, but rather, its diameter dictates the curvature connecting the high and low density points. The one dimension density profile was constructed by repeating this curved density profile of the individual layer 25 times (Figure 4a). The corresponding fit of the reflectivity data using the typical Parratt formalism is shown in Figure 4b. Comparing with the result of Figure 3, we now have a better fit in the low q regime up to the regime immediately after the first Bragg peak. Thus, the reflectivity from multiple length scales can be obtained from one periodic structure and the curvature within the structure. It is also important to note that the large unoriented region in the interior of the film, between the oriented ordered

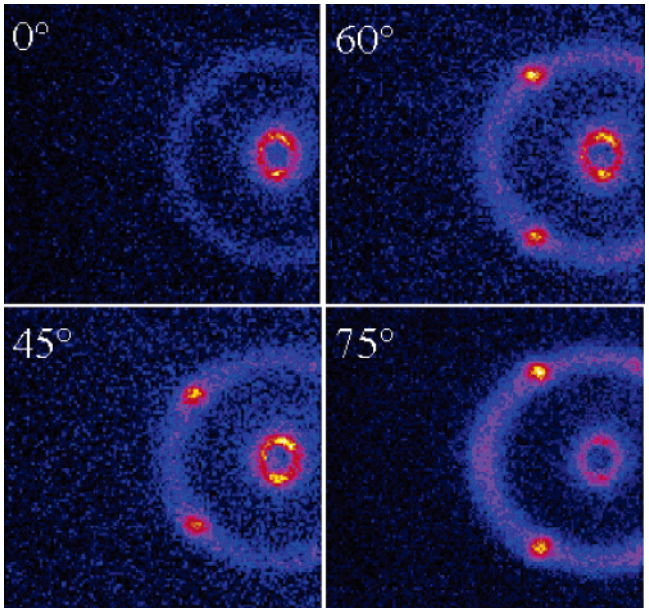

Figure 5. SANS profiles for various sample tilts relative to the film normal.

cylinders, does not appear to introduce any additional features in the low-resolution reflectivity profile. It is only possible to determine the existence of this disordered interior region from the total film thickness value deduced from the high-resolution reflectivity result (Figure 1b). Improved fits of the reflectivity data could be obtained by damping the amplitude of the repeating scattering length density toward the center of the film, for example, by introducing a decay length in an exponential term as suggested by Fredrickson for block copolymers.[8] These improved fits, however, would contain little data that would not be obtained from the simple fits of Figure 1. As such, we have not continued to add parameters to improve the reflectivity fit.

To elucidate further the 3-D organization of the mesoporous sample, SANS data were collected with the incident beam normal to the wafer plane and at select oblique angles. Typically, only the normal incident beam is used for the SANS characterization of thin films, only probing the in-plane correlations.[11] However, use of several oblique angles as well as the normal incident allows for the development of a 3-D representation of the film morphology. Figure 5 shows 2-D images of the scattering pattern obtained at a tilt angle, α, of 0, 45, 60, and 75° where α is the angle between the SANS beam and the normal of the sample surface. At 0° (normal incident), there is a scattering ring corresponding to spacing of the mesopores. The isotropic nature of the scattering in the azimuthal direction indicates that there is no long-range in-plane order in the film. If the sample is tilted to 45° or greater, the scattering ring remains, but high intensity spots appear on the ring at discrete azimuthal angles. These spots clearly manifest the existence of a 3-D ordered structure within the sample. A quantitative analysis of Figure 5 shows that the azimuthal angle between the two peaks within the ring increases with sample tilt. However, the magnitude of q of the peaks stays unchanged at 0.0599 $Å^{-1}$ regardless of the tilt. Furthermore, it shows that the scattering rings are actually ellipses at all the inclined incident angles. The short axis remains at a value of 0.0572 $Å^{-1}$ independent of the incident angle. Whereas the long axis increases with the sample tilt, it increases from the value of 0.0572 to 0.0676 $Å^{-1}$ as the sample tilts from the normal

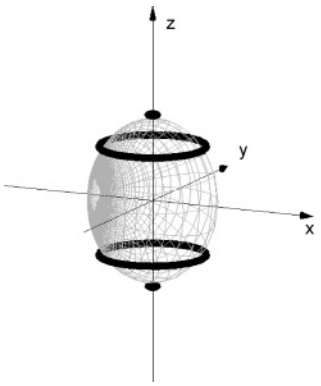

Figure 6. Fourier space representation of the mesoporous film determined from SANS.

incident condition toward 90°. It is noteworthy that 0.0676 $Å^{-1}$ marks the position of the first Bragg peak of Figure 1.

On the basis of the previous incident angle dependent SANS information, several important characteristics of the 3-D scattering pattern of this sample become clear. The 3-D scattering pattern is composed of three structural elements: (1) ellipsoid with a long axis ($q = 0.0676$ $Å^{-1}$) parallel to the surface normal and a short axis ($q = 0.0572$ $Å^{-1}$) parallel to the film surface, (2) two high-intensity spots at the ends of the long axis corresponding to the first Bragg peak observed in the SXR data in Figure 1, and (3) a pair of scattering rings with their centers located on the long axis of the ellipsoid. This type of 3-D structure in the Fourier space is illustrated in Figure 6, where the *z*-axis is along the film thickness direction. At a tilt angle α, the observed scattering pattern is simply the intercept of this 3-D structure with a plane (Ewald sphere) tilted at the angle α with respect to the $x-y$ plane. At sufficiently large tilting angles, the scattering rings (3) are intercepted, which gives rise to a pair of peaks or high-intensity spots within the ring as observed in the tilted samples in Figure 5. The conical angle between the rings and the long axis was determined to be 55.7° from detailed analysis of the scattering profiles at the tilt angles. It is noteworthy that this conical angle is slightly less than 60°, suggesting a slightly compressed hexagonal packing of the tubes. The aspect ratio of the ellipsoid is 1.182 representing the compression ratio. By assuming that the compression of the hexagonal lattice along the film thickness direction does not induce any expansion along the film surface, one can readily calculate the value of q (h,k). Its value turns out to be 0.0599 $Å^{-1}$, a value identical to that experimentally observed. The structural information expressed in the Fourier space representation (Figure 6) corresponds to the following real-space structures. The ellipsoid (1) can be described as a collection of randomly oriented objects. In addition, the object spacing is slightly compressed along the film thickness direction. The high intensity dots at the ends of the ellipsoid (2) correspond to (0,l) diffraction of mesopore crystals. The rings on the ellipsoid (3) is consistent with the existence of planarly ordered layers with a random in-plane orientation, and the (h,k) type diffraction of the ordered layers gives rise to the ring.

On the basis of the micrograph in Figure 2, the basic structural block in the film is a cylindrical pore or hollow tube. 3-D packing of cylindrical pores can be specified with two indices instead of three. These pores tend to arrange themselves in nearly hexagonal close packing with a packed plane parallel to the sample surface. This type of structure has been commonly observed in block copolymers and other templated ordered systems in thin film geometries. However, for simple hexagonal packing, the conical angle between the rings and the long axis in the Fourier space should be 60° instead of the measured value of 55.7°. This angular difference indicates that the hexagonal order is compressed along the surface normal within the ordered layers. The anisotropy due to the shrinkage can be confirmed independently using SXR and normal incidence SANS. From SXR, the spacing between the (0,2) planes is 92.97 Å, while the peak position at normal incidence from SANS is at $q =$ 0.0572 $Å^{-1}$, which is assigned to (1,1) diffraction. The corresponding conical angle based on the previous (1,1) and (0,2) lattice dimensions is found to be 55.7°. The compression of the hexagonal order indicated by the conical angle is not unexpected as anisotropic shrinkage due to confinement by the supporting substrate has been previously observed during porogen removal.[12]

We now return to the determination of pore diameter using a combination of the SANS and SXR. The porosity of the sample was determined using toluene vapor as a probe molecule. The capillary condensation within the pores when exposed to saturated vapor causes a shift in the critical edge of the SXR measurement due to the increased average electron density of the film.[22] From the amount of electron density increase and the density of toluene, the porosity of the sample is determined to be 49%. From the porosity and lattice dimensions determined from SANS, the cylindrical pore diameter is estimated to be 82 Å. This is slightly larger than expected from the TEM micrographs, presumably due to microporosity in the pore wall.[11,23] SANS and SXR are capable nondestructive characterization tools that provide insight into the structure of mesoporous thin films.

Conclusions

The pore structure and orientation of mesoporous films was elucidated using a combination of SANS and SXR. The structure and orientation of the mesoporous film was determined from SANS measurements at various incident angles. By rotating the sample, the 3-D representation of the film structure in Fourier space is determined to consist of an ellipsoid with high intensity points at its end and two rings encircling the outside of the ellipsoid. These structural details in real space correspond to slightly compressed randomly distributed scattering objects, (0,l) diffraction, and ordered layers in the *z*-direction, respectively. Additionally, the ordered mesotubes are not hexagonally packed but slightly compressed with a conical angle of 55.7°. Additional structural information can be elucidated from SXR measurements. For the cylindrical mesoporous material examined, the number of layers oriented with the interfaces is determined from the width of the Bragg peak. The SXR result corresponds well to a TEM micrograph of the material. Additionally, there was a sharp decrease in the reflectivity at q slightly larger than the Bragg reflection. This decrease was found to be a result of a second length scale due to the cylindrical mesopores. This decrease can be fit either by scattering expressions developed by Ruland and Smarsly[17] or with typical reflectivity expressions where the cylindrical size is determined by the curvature between the repeating regions of high and low scattering length density.

Acknowledgment. B.D.V. acknowledges financial support from the NIST/NRC postdoctoral program. The authors thank Derek Ho and C. J. Glinka for their assistance with the SANS measurements as well as Brendan Foran of SEMATECH for the TEM microscopy work. Certain commercial equipment and materials are identified in this paper to specify adequately the experimental procedure. In no case does such identification

imply recommendations by the National Institute of Standards and Technology nor does it imply that the material or equipment identified is necessarily the best available for this purpose.

References and Notes

(1) Davis, M. E. *Nature* **2002**, *417*, 813−821.

(2) Kresge, C. T.; Leonowicz, M. E.; Roth, W. J.; Vartuli, J. C.; Bach, J. S. *Nature* **1992**, *331*, 698−699.

(3) Zhao, D.; Feng, J.; Huo, Q.; Melosh, N.; Fredrickson, G. H.; Chmelka, B. F.; Stucky, G. D. *Science* **1998**, *279*, 548−552.

(4) Yang, P.; Zhao, D.; Margolese, D. I.; Chmelka, B. F.; Stucky, G. D. *Nature* **1998**, *396*, 152−155.

(5) Brinker, C. J.; Lu, Y.; Sellinger, A.; Fan, H. *Adv. Mater.* **1999**, *11*, 579−585.

(6) Trau, M.; Yao, N.; Kim, E.; Xia, Y.; Whitesides, G. M.; Aksay, I. A. *Nature* **1997**, *390*, 674−676.

(7) Fasolka, M. J.; Mayes, A. M. *Annu. Rev. Mater. Res.* **2001**, *31*, 323−355.

(8) Fredrickson, G. H. *Macromolecules* **1987**, *20*, 2535−2542.

(9) Pai, R. A.; Humayan, R.; Schulber, M. T.; Sengupta, A.; Sun, J.-H.; Watkins, J. J. *Science* **2004**, *303*, 507−510.

(10) Schmidt, R.; Hansen, E. W.; Stocker, M.; Akporiaye, D.; Ellestad, O. H. *J. Am. Chem. Soc.* **1995**, *117*, 4049−4056.

(11) Smarsly, B.; Goltner, C.; Antonietti, M.; Ruland, W.; Hoinkis, E. *J. Phys. Chem. B* **2001**, *105*, 831−840.

(12) Grosso, D.; Balkenende, A. R.; Albouy, P. A.; Ayral, A.; Amenitsch, H.; Babonneau, F. *Chem. Mater.* **2001**, *13*, 1848−1856.

(13) Choma, J.; Jaroniec, M.; Burakiewicz-Mortka, W.; Kloske, M. *Appl. Surf. Sci.* **2002**, *196*, 216−223.

(14) Zhou, X.-L.; Chen, S.-H. *Phys. Rep.* **1995**, *257*, 223−348.

(15) Ankner, J. F.; Maikrzak, C. F. *Proc. SPIE* **1992**, *1738*, 260. Parratt, L. G. *Phys. Rev.* **1954**, *95*, 359−369.

(16) Russell, T. P. *Mater. Sci. Rep.* **1990**, *5*, 171−271. Wu, W.-l. *J. Chem. Phys.* **1993**, *98*, 1687−1694.

(17) Ruland, W.; Smarsly, B. *J. Appl. Crystallogr.* **2005**, *38*, 78−86.

(18) Holy, V.; Baumbach, T. *Phys. Rev. B* **1994**, *49*, 10668−10676.

(19) Jiang, X. M.; Metzger, T. H.; Peisl, J. *Appl. Phys. Lett.* **1992**, *61*, 904−906.

(20) Rafaja, D.; Fuess, H.; Simek, D.; Kub, J.; Zweck, J.; Vacinoca, J.; Valvoda, V. *J. Phys.: Condens. Mater.* **2002**, *14*, 5303−5314.

(21) de Wames, R. E.; Sinha, S. K. *Phys. Rev. B* **1973**, *7*, 917.

(22) Lee, H.-J.; Lin, E. K.; Bauer, B. J.; Wu, W.-l.; Hwang, B. K.; Gray, W. D. *Appl. Phys. Lett.* **2003**, *82*, 1084−1086.

(23) Imperor-Clerc, M.; Davidson, P.; Davidson, A. *J. Am. Chem. Soc.* **2000**, *122*, 11925−11933.